JASA ARTICLE

Aeroacoustic investigations of a rotor-beam configuration in small-size drones[a)]

Jose Rendón-Arredondo,[1,b)] Emma Vella,[1,2] Andrea Arroyo Ramo,[1] Michel Roger,[3] Romain Gojon,[2] Thierry Jardin,[2] and Stéphane Moreau[1]

[1]*Université de Sherbrooke, Sherbrooke, Québec J1K2R1, Canada*

[2]*ISAE - SUPAERO, Université de Toulouse, Toulouse, France*

[3]*Ecole Centrale de Lyon, Ecully 69134, France*

ABSTRACT:

Various aeroacoustic mechanisms involved in a rotor-beam configuration typically encountered in small-size drones in hover conditions are investigated both numerically and analytically, complemented with experimental data. High-fidelity lattice-Boltzmann method (LBM) simulations are performed on the complete experimental setup, capturing both the aerodynamic and the acoustic features of the configuration. The far-field noise is obtained by applying the Ffowcs Williams and Hawkings (FW-H) acoustic analogy. The rotor noise is also modeled as the sum of thickness noise, steady and unsteady loading noise corresponding to potential interactions between the blades and the beam. The analytical model of rotor noise relies on a strip theory, combining input velocity profiles from LBM and Sears's blade response function for each strip, and the FW-H analogy formulated in the frequency domain. The beam noise is modeled using a similar strip theory and a response model to the circulation of passing blades, based on the incompressible potential flow theory around a circular cylinder. Aerodynamic and acoustic results from the simulation and the models are in good agreement with measurements. Unsteady loading noise is found dominant for all tones for the present rotor-beam configuration corresponding to a small chord-to-beam diameter ratio. The three-dimensional directivities of some sound harmonics also have a unique wavy pattern in the rotor plane.

NOMENCLATURE

B Number of rotor blades
c_0 Speed of sound [m/s]
c Airfoil chord [m]
$C(x)$ Theodorsen function
d Distance between the top of the beam and the rotor plane [m]
D_b Beam diameter [m]
J_n Bessel function of order n
k Loading harmonic
k_{mB} $mB\Omega/c_0$, wavenumber related to the mth harmonic of the BPF [rad/m]
L Rotor-beam separation distance [m]
m Sound harmonic
n_b Number of beams equally distributed along the azimuth
(r, ϕ) Polar coordinates
r_{root} Root radius [m]
r_{tip} Tip radius [m]
R Observer distance from the rotor center [m]
RPM Rotation per minute [min^{-1}]

t Time [s]
U_z Rotor induced velocity [m/s]
U_r Ωr, velocity at the blade section r [m/s]
Z $X + iY$, complex coordinate
Z_v $X_v + iY_v = \Omega rt + iL$, vortex complex coordinate
α Blade pitch angle [deg.]
γ Blade stagger angle with respect to the rotor axis [deg.]
Γ Vortex circulation [m2/s]
θ_{exp} Latitude observer position considered in the experiments [deg.]
Θ $\pi/2 - \theta_{exp}$, latitude observer position considered in the model [deg.]
ρ_0 air ambient density [kg/m3]
ϕ_{exp} azimuth observer position considered in the experiments [deg.]
Φ $\pi - \phi_{exp}$, azimuth observer position considered in the model [deg.]
Ω rotor angular speed [rad/s]

[a)]This paper is part of a special issue on Advanced Air Mobility Noise: Predictions, Measurements, and Perception.
[b)]Email: jose.manuel.rendon.arredondo@usherbrooke.ca

I. INTRODUCTION

The presence and use of unmanned air vehicles (UAVs) is likely to increase in the near future. They are present in a wide range of applications and industries such as entertainment, security, military operation, and delivery to name just

a few. These sectors usually prefer the use of multicopters because of their stability, agility, and versatility. As a consequence, these technologies are prompt to become more present in urban environments and trigger an increase in noise pollution. As for any rotating-blade system, their noise comprises tonal and broadband components. The former is known to be dominant and is mainly due to periodic rotor-rotor and rotor-airframe interactions, which radiate at the blade passing frequency (BPF) and its harmonics (Lauzon et al., 2023). The evaluation and study of rotor noise started in the first half of the 20th century with studies such as the ones developed by Gutin (1948) and later by Ffowcs Williams and Hawkings (1969). However, most of them focused on high Reynolds number helicopters rotors or aircraft propellers. Nevertheless, multicopters, and in general UAVs, operate at lower to moderate Reynolds numbers, which trigger different flow regimes and therefore change the main involved noise sources.

Recently, isolated rotors inside this Reynolds number range have been studied both experimentally and numerically. Gojon et al. (2021) developed a database on low Reynolds number rotors operating in hover and derived scaling laws for the different noise sources. The trailing-edge noise was found to be the main contributor to high-frequency noise similar to the experimental work performed by Zawodny et al. (2016). Numerically, several low and high-fidelity approaches have been used. Regarding the former, the non-linear vortex lattice method has been used by Jo et al. (2019) to evaluate the effect of the number of blades on low-speed rotors. For the latter, Shenoy et al. (2024) developed a high-resolution Navier-Stokes (NS) compressible large eddy simulation (LES) to study the flow topology and noise radiation of hovering rotors. Similarly, multiple studies have used the hybrid lattice-Boltzmann method (LBM) very-large-eddy-simulation (VLES). For example, Romani et al. (2022) and Casalino et al. (2022) studied the effect of using a zigzag trip and a new transitional model to properly predict the noise of these configurations. The comparison between LBM/VLES and NS/LES methods has also been addressed by Rendon-Arredondo et al. (2024), showing the advantage of the former regarding the computational time and the geometries that can be accounted for, making it suitable to study these types of systems.

In addition to isolated rotors, several studies have been achieved on more realistic configurations representative of rotor-airframe interaction. Zawodny and Boyd (2017) studied the case of a cylindrical beam placed in the wake of a rotor both experimentally and numerically. They showed that the noise emitted by this configuration is highly directional, with the beam noise dominating in the rotor plane, where the greatest emission occurs orthogonal to the beam. Gojon et al. (2023) observed experimentally a similar trend. They found two main humps in the far-field spectra: the first hump, centered at $5 \times$ BPF, is related to the beam noise, while the origin of the second one, centered at a higher frequency of $25 \times$ BPF, is still unknown. Then, Doué et al.

(2023) performed numerical simulations on a similar configuration using an incompressible implicit LES method coupled with a Ffowcs-Williams and Hawkings (FW-H) acoustic analogy with integration on the solid surfaces (impermeable formulation). By separating the contributions of the rotor and the beam, the beam was confirmed to be responsible for the first hump observed experimentally. Again in a similar rotor-airframe configuration, Kim et al. (2024) performed an aerodynamic analysis using LBM simulations, and obtained some acoustic results using the permeable formulation of the FW-H analogy. They captured the tip-vortex breakdown phenomenon and the transition into a turbulent wake. They found very small differences between permeable and impermeable FWH methods stressing that, in their configuration, the unsteady loading component due to rotor-airframe interaction is dominant compared to the acoustic scattering.

Rotor-beam interaction has also been addressed theoretically. Roger et al. (2023) derived an analytical model for the steady-loading and unsteady-loading noise of rotor blades due to operation through the potential field of a cylindrical beam. The beam contribution was addressed as a diffraction effect and accounted for using a cylinder-scattering model. In continuation, Rendon et al. (2024) performed a numerical and analytical study to assess the effect of the rotor-beam distance on the flow field and the acoustic signature. The data obtained with the LBM simulation was then used as input to the analytical model, leading to an overall overprediction of the noise using this approach. Wu et al. (2022) also developed an analytical method to estimate the unsteady-loading on both the propeller blades and the beam. Similarly, the analytical model slightly overestimated the amplitude of the pressure impulse radiated in the far field. A similar approach was followed in a recent work by Vella et al. (2024) where the interaction of a rotor-beam configuration was studied to gain further insight into the noise generating mechanisms and the associated noise directivity.

Despite these studies, there is a lack of theoretical work on rotor-beam interaction noise and assessment of analytical models against numerical and experimental data. This paper focuses on a diametral rotor-beam configuration simulated using the commercial software Simulia PowerFlow which permits one to validate the analytical model for the prediction of the far-field noise. First, the experimental setup used to validate the simulations is presented, followed by the description of the flow solver implemented. Then, the blade potential-interaction noise model and the beam potential-interaction noise model are detailed. Aerodynamic and acoustic results are then compared using the different approaches already explained. Finally, conclusions are given from the results.

II. EXPERIMENTAL SETUP

The rotor-beam arrangement is installed in the anechoic room of Ecole Centrale de Lyon (ECL), with dimensions $6.4 \times 4.6 \times 3.8 \, \text{m}^3$ and a cut-off frequency of 100 Hz. The
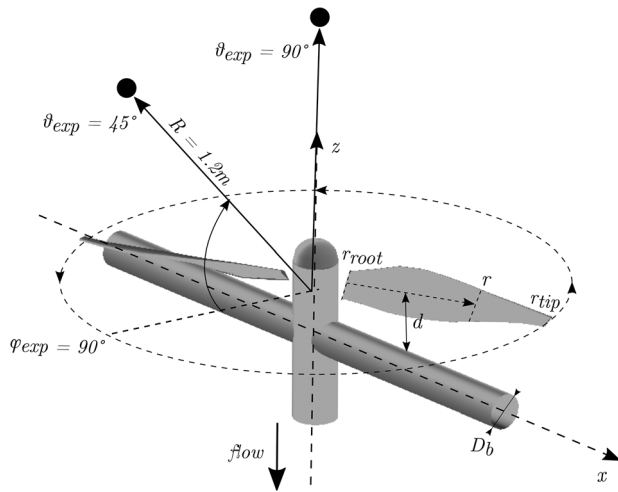
FIG. 1. Experimental setup at ECL. The two microphones are represented by the black dots.

configuration is mounted on top of the motor unit, placed at the top of a vertical mast of circular cross section. The cylindrical beams of diameter $D_b = 32$ mm, are supported by two vertical arms placed on each side of the mast, at a distance $d = 14$ mm downstream of the rotor plane, d being the distance between the top of the beam and the rotor plane (see Fig. 1). As the setup is installed at limited distances to the walls and ground (0.72 m above the ground), there is some ground effects generating an amplitude modulation at the BPF harmonics. Yet, the potential interaction noise is expected to be much higher as shown in Rendon-Arredondo *et al.* (2024). The setup installation is fully detailed in Roger *et al.* (2023) and the main setup characteristics are summarized in Table I. For the acoustic measurements, two 1/2-in. B&K microphones, type 4189, are placed at $R = 1.2$ m away from the rotor center, at $\phi_{\exp} = 90°$ (corresponding to the vertical plane orthogonal to the beam axis), $\theta_{\exp} = 45°$, and $\theta_{\exp} = 90°$. The microphones distance ensures geometrical far-field conditions, as well as the acoustic far-field conditions, beyond 250 Hz. Acoustic signals are acquired during 30 s. An averaged spectrum, with a resolution of 1 Hz, is obtained by averaging spectra on 1 s time-window.

III. NUMERICAL SETUP

The LBM solver PowerFLOW 6-2021 is used to compute the aerodynamics and acoustics of the aforementioned rotor-beam configurations. It solves the particle distribution function of the Boltzmann equation in a discrete form (Chen *et al.*, 1992; Chen *et al.*, 2004). The probability function of a particle at a given position and speed is then related to the external forces and a collision operator that describes the collision of the particles. The latter is modeled with a modified Bhatnagar-Gross-Krook (BGK) approximation (Bhatnagar *et al.*, 1954). The discretization of the Boltzmann equation is made on cubic elements called lattices (voxels). The D3Q19 lattice consisting of 19 discrete velocities directions in three dimensions is used.

To maintain a reasonable computational time and number of voxels, the hybrid approach LBM/VLES is selected for the present study. A two-equation RNG $\kappa - \epsilon$ turbulence model is implemented with a second-order time-explicit finite-difference scheme to account for the unresolved turbulent scales. In addition, an effective turbulent relaxation time is calculated following the work of Yakhot and Orszag (1986). Moreover, a pressure-gradient extended wall model is used to account for the non-slip boundary condition at the solid walls (Teixeira, 1998). To simulate the rotational motion of the rotor, a body-fixed local reference frame (LRF) is used. It is defined by generating a rigid grid based on an axisymmetric volume that rotates with the geometry, so there is no relative motion between the LRF grid and the rotor.

The computational fluid domain, shown in Fig. 2, mimics the anechoic chamber of ECL, with VR4 (Variable Resolution 4) having the exact dimensions of the facility. The rotor-beam geometry is aligned with a solid wall defining the floor of the chamber and five boundaries with an increased viscosity value to mimic the sponge cones. Three damping zones [delimited by the blue lines in Fig. 2(a)] extend outwards of this region to dissipate acoustic waves and minimize reflections from the external boundaries by imposing a higher viscosity value. This value is calculated as the ratio of lattice viscosity and lattice temperature as defined by Li *et al.* (2004), and has a value of 0.001, 0.01, and 0.05 applied inward for the first three damping zones. For the external boundaries of VR1, a value of 0.5 is imposed together with an extra anechoic outer layer boundary condition to improve the effect of the damping and guarantee the lack of reflected noise. Free-stream static pressure is imposed in the outer walls (aligned with all outer slip walls at the external boundaries of VR1) and the outlet. An additional zero velocity is imposed at the inlet boundary to fully define the hover condition found in the experiments. A VR mesh strategy is used to discretize the computational domain. A total of 13 regions are used, where the grid size changes by a factor of two for adjacent resolution regions. To reduce the number of grid points, the two finest zones correspond to an offset of the rotor and beam geometry. The following refinement regions are disks placed on the near wake, as explained in Rendon *et al.* (2024) and shown in Fig. 2(b). The minimum voxel size is 0.05 mm, achieving an average dimensionless distance to the wall $y^+ \approx 5$

TABLE I. ECL experimental setup characteristics.

Source-obs. dist.	Rotor	Root/Tip-radius	RPM	Reynolds nb.	Beam diam.	Rotor-beam dist.
$R = 1.2$ m	APC $7 \times$ C5-E	0.023/0.088 m	6420	3.71×10^4 (at $0.8\,r_{tip}$)	$D_b = 32$ mm	$d = 14$ mm

J. Acoust. Soc. Am. **158** (2), August 2025
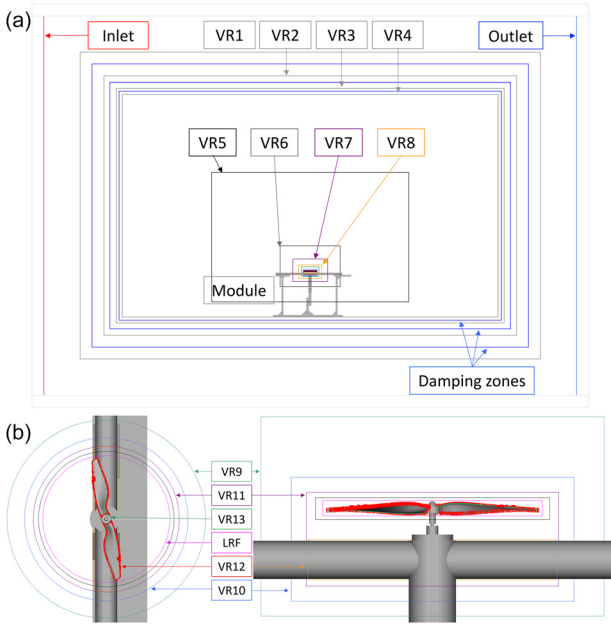
Rendón-Arredondo *et al.*   1093

FIG. 2. Computational domain and refinement zones for the ECL experimental set-up; (a) first 8 VR regions and (b) last 5 VR regions with the LRF.

(maximum y^+ at the blade tip of about 10), and implying a quasi wall-resolved LES. A total of 120×10^6 equivalent voxels are generated for the present case. The intermediate VR regions have a voxel size based on the previous grid sizes reported by Moreau and Sanjose (2016) in applications at a similar tip Reynolds number.

Forces, velocity, and pressure are recorded on the surfaces of the rotor and beam with a sampling frequency of 19 kHz. The former is used to calculate the inputs of the analytical model presented in Sec. IV. Furthermore, the latter is used to perform a hybrid approach by applying the solid formulation of the Ffowcs Williams and Hawkings (FW-H) acoustic analogy. The FW-H solution is based on a forward-time solution of the 1A formulation (Farassat and Succi, 1980; Casalino, 2003). A surface distribution of acoustic monopoles and dipoles is considered, while the quadrupole contribution is neglected. This approach is valid as the first two are associated with the thickness and loading noise terms, which dominate for propellers operating at low blade-tip Mach number. Far-field noise is then computed using a spherical array of 216 microphones with a spacing of 20° and 15° in the θ and ϕ directions, respectively.

The simulation is initialized with the flow field obtained from a previous case that used a coarser mesh. The latter ran for around 30 s of physical time and showed that there is no major recirculation within the anechoic environment. The simulation was then continued on the refined mesh for an additional 40 revolutions, which corresponds to 0.375 s. Convergence was achieved when the rotor forces and the far-field pressure had stabilized, after 8 revolutions, as already shown by Rendon et al. (2024). After this transient, the results are sampled for 32 revolutions for the force and pressure data.

IV. ANALYTICAL MODELS

Analytically, the rotor noise is obtained by summing the thickness noise [using the formulation in Hanson and Parzych (1993)], the steady loading noise and the unsteady loading noise. The two latter are detailed in the following, as well as the beam unsteady loading noise. The two analytical models presented are both potential-interaction noise models. The inputs needed for the models are the axial velocity profiles induced by the rotor and the thrust and torque distributions. They are presently obtained from the LBM simulation. Yet, it is also possible to calculate these inputs with a blade element momentum theory (Leishman, 2006).

A. Blade potential–interaction noise

The sound pressure generated in the far-field, at the mth harmonic of the BPF, by rotor blades experiencing steady and unsteady loading (induced by the presence of a diametrical beam) is based on Hanson's work on noise of rotors (Hanson and Parzych, 1993). Considering hovering conditions and assuming the radial loading negligible, Hanson's formula is simplified as follows:

$$p_{mB}(\boldsymbol{x},t) = \frac{-\mathrm{i}k_{mB}B}{4\pi R} \sum_k e^{\mathrm{i}[(mB-kn_b)(\Phi-\pi/2)+mB\Omega(R/c_0-t)]}$$

$$\times \int_{root}^{tip} \mathrm{J}_{mB-kn_b}\left(mB\frac{\Omega r}{c_0}\sin(\Theta)\right)$$

$$\times \left[\frac{mB-kn_b}{rk_{mB}}F_{blade,\phi}^{(k)}(r) + \cos(\Theta)F_{blade,z}^{(k)}(r)\right]\mathrm{d}r,$$

$$(1)$$

with $(R,\Theta,\Phi) = (R,\pi/2 - \theta_{\exp}, \pi - \phi_{\exp})$ the observer coordinates, and n_b corresponding to the number of beams equally distributed along the azimuth, downstream of the rotor. The latter is $n_b = 2$ as the beam is diametrical. $F_{blade,z}^{(k)}$ and $F_{blade,\phi}^{(k)}$ in Eq. (1) are the kth harmonics of the axial and tangential forces acting on one rotor blade, respectively. Steady loading noise is related to the steady part of these forces, $F_{blade,z}^{(0)}$ and $F_{blade,\phi}^{(0)}$, and higher loading harmonics k are related to the unsteady part. Note that these forces are calculated at discrete radii resorting to a strip theory, and that this formulation considers the blade chord acoustically compact. The latter approximation is reasonable up to $f = 5540\,\mathrm{Hz}$, i.e., $25 \times \mathrm{BPF}$, according to the compactness criterion described by Amiet (1975).

The kth harmonics of the axial and tangential forces are directly deduced from the harmonics of lift per unit span L_k, themselves derived from Sears's theory (Sears, 1941) applied to unwrapped radial cuts of the rotor-beam configuration

$$L_k(r) = \pi\rho_0 c U_r w_k(r)\overline{\left[C(\sigma)(\mathrm{J}_0(\mu) - \mathrm{i}\mathrm{J}_1(\mu)) + \frac{\mathrm{i}\sigma}{\mu}\mathrm{J}_1(\mu)\right]},$$

$$\sigma = \frac{kn_b\Omega c}{2U_r}; \quad \mu = \frac{\mathrm{i}kn_b c}{2r}e^{-\mathrm{i}\gamma},$$

$$(2)$$

with the overbar indicating the complex conjugate, and σ and μ modified for a diametrical beam, using the term n_b. The harmonics L_k in Eq. (2) are the response of the corresponding blade section to the potential field generated by the presence of n_b beams downstream of the rotor. In this equivalent two-dimensional (2D) problem, the velocity distortion, i.e., upwash distortion, is obtained from the solution of the incompressible potential flow problem around n_b 2D circular cylinders. The flow velocity corresponds to the axial rotor-induced velocity U_z, which is an acceptable approximation given the very moderate swirl induced by the rotor in the present study. Then the response in lift of the corresponding blade section, modeled as a 2D flat plate with a velocity Ωr, is obtained by applying the resulting upwash distortion, using the Sears's theory. The upwash harmonics w_k are derived from Wu et al. (2022) and adapted using the method described by Parry (1988); Sanjose et al. (2017) for the potential field generated by the presence of n_b beams

$$w_k(r) = \frac{-\mathrm{i}kn_b^2 U_z(r)D_b^2}{8r^2}\mathrm{e}^{(-n_b k/r)L + \mathrm{i}\gamma}, \quad k \geq 1, \qquad (3)$$

with $L = d + D_b/2$ the distance between the rotor plane and the beam axis.

B. Beam potential–interaction noise

The sound pressure radiated in the far-field, at the mth harmonic of the BPF, by n_b beams experiencing a velocity distortion each time a rotor blade passes nearby, is derived from Lowson's work on noise of rotor-stator stages in compressors (Lowson, 1969)

$$p_m(\boldsymbol{x},t) = \frac{-\mathrm{i}k_{mB}n_b}{4\pi R}\sum_k \mathrm{e}^{\mathrm{i}[(mB-kn_b)(\Phi - \pi/2) + mB\Omega(R/c_0 - t)]}$$

$$\times \int_{root}^{tip} \mathrm{J}_{mB-kn_b}\left(mB\frac{\Omega r}{c_0}\sin(\Theta)\right)$$

$$\times \left[\frac{mB - kn_b}{rk_{mB}}F_{beam,\phi}^{(m)}(r) + \cos(\Theta)F_{beam,z}^{(m)}(r)\right]\mathrm{d}r, \qquad (4)$$

with $F_{beam,z}^{(m)}$ and $F_{beam,\phi}^{(m)}$ the mth harmonics of the axial and tangential forces acting on one beam.

Similarly to the case of the rotor, a 2D model based on unwrapped radial cuts of the rotor-beam configuration is built. The loading fluctuations on one beam at each strip, are obtained from the solution for an incompressible potential flow problem around a 2D circular cylinder. This modeling is suggested by Wu et al. (2022) for a radial configuration. The reader can refer to Vella et al. (2024) for a visual representation of the coordinate system. At a given section r, a complex potential $f(Z)$ produced by a vortex with circulation $\Gamma(r) > 0$ (modeling the rotor blade section) and a free-stream flow velocity $U_z(r)$ (corresponding to the axial rotor-induced velocity at this section) is introduced, with the complex coordinate $Z = X + \mathrm{i}Y$. The vortex is located at

$X = X_v = \Omega r t$, as the vortex moves with a velocity Ωr in the X-direction, and $Y = Y_v = L = d + D_b/2$ corresponding to the distance between the vortex and the cylinder axis. Using Milne Thompson's circle theorem, the following formulation considers the presence of the circular cylinder:

$$f(Z) = -\frac{\mathrm{i}\Gamma(r)}{2\pi}\ln(Z - Z_v) + \frac{\mathrm{i}\Gamma(r)}{2\pi}\ln\left(\frac{D_b^2}{4Z} - \overline{Z_v}\right)$$

$$+ \mathrm{i}U_z(r)\left(Z - \frac{D_b^2}{4Z}\right). \qquad (5)$$

Then, once the velocity components, u and , are computed from the derivatives of the velocity potential, the pressure within the fluid is deduced everywhere on the 2D section of interest, using the unsteady Bernoulli theorem

$$p(Z) - p_\infty = \frac{1}{2}\rho_0(U_z(r)^2 - U^2)$$

$$+ \frac{\rho_0\Gamma(r)\Omega r}{2\pi}\Re\left(\frac{\mathrm{i}}{\overline{Z_v}} + \frac{\mathrm{i}}{Z_v - Z} - \frac{\mathrm{i}}{\overline{Z_v} - \frac{D_b^2}{4Z}}\right) \qquad (6)$$

with $U^2 = u^2 + v^2$. The wall pressure on the surface of the circular cylinder is then extracted, thus taking $Z = D_b\mathrm{e}^{\mathrm{i}\theta_b}$, with θ_b corresponding to the second cylindrical coordinate. By projections on the axes of interest, the axial and tangential forces per unit length, exerted on the beam for one blade passage, are obtained as

$$\begin{cases} \hat{F}_{beam,\phi}(r,t) = \frac{D_b}{2}\int_0^{2\pi} p\left(\frac{D_b}{2}\mathrm{e}^{\mathrm{i}\theta_b}\right)\cos(\theta_b)\mathrm{d}\theta_b, \\[2mm] \hat{F}_{beam,z}(r,t) = \frac{D_b}{2}\int_0^{2\pi} p\left(\frac{D_b}{2}\mathrm{e}^{\mathrm{i}\theta_b}\right)\sin(\theta_b)\mathrm{d}\theta_b. \end{cases} \qquad (7)$$

Then, the contribution of individual vortices (one vortex for each blade section) can be summed if and only if they are separated by a large distance, i.e., the potential interaction effect induced by a blade passage is not affected by the potential interaction effect of the following blade passage. In this case, the summed contributions of an infinite number of vortices is relevant for $r > 0.5\ r_{tip}$, where the distance between two vortices starts to be large enough. In the following equation, only the expression of the tangential force is developed as the expression for the axial force is similar:

$$F_{beam,\phi}(r,t) = \sum_{n=-\infty}^{\infty} \hat{F}_{beam,\phi}\left(r, t + \frac{2\pi}{B\Omega}n\right)$$

$$= \sum_{k=-\infty}^{\infty} F_{beam,\phi}^{(k)}(r)\mathrm{e}^{-\mathrm{i}kB\Omega t}. \qquad (8)$$

The loading harmonics acting on one beam are finally computed as the Fourier coefficients of the loading fluctuations $F_{beam,\phi}(r,t)$. These loading harmonics are then used to compute the tonal noise radiating by the n_b beams using Eq. (4).

J. Acoust. Soc. Am. 158 (2), August 2025

Rendón-Arredondo et al. 1095

It is relevant when the n_b beams have neither aerodynamic nor acoustic interactions between each other, i.e., the distance between a beam and the following one is large enough.

V. AERODYNAMIC RESULTS

A. Unsteady blade forces

Figure 3 shows the signals of the unsteady force on one blade in the axial [Figs. 3(a)–3(c)] and tangential [Figs. 3(d)–3(f)] directions. Note that the radial component of the force is also calculated using the LBM simulation and is found to be at least one order of magnitude lower than the other two components. Thus, this force can be neglected, and the 2D model assumption is overall valid. The black line represents the results obtained by the LBM simulation, and the gray dashed line the results obtained with the blade potential-interaction model. For both approaches, the blade span is divided into 20 equally spaced strips. This ensures that each of them is acoustically compact, similarly to the assumption made for the blade chord. Three different radial locations are analyzed, specifically at mid span [Figs. 3(a) and 3(d)], at $r/r_{tip} = 0.8$ [Figs. 3(b) and 3(e)], and at $r/r_{tip} = 0.9$ [Figs. 3(c) and 3(f)].

As seen, each blade experiences two fluctuations per rotation, associated with the presence of the diametrical beam. These fluctuations are characterized by an increase in the thrust produced by the blade as a consequence of the reduced axial velocity and an increase in angle of attack. First, looking at the location $r/r_{tip} = 0.5$, the model overpredicts the two force components, with the axial force having a higher amplitude of loading fluctuation than the tangential force. Moving to the location $r/r_{tip} = 0.8$, the tangential force is still overpredicted by the analytical model, while a small under-prediction is obtained for the axial force. This

location is also characterized by sharper loading fluctuations that are caused by a higher azimuthal velocity of the blade section together with a smaller chord-to-beam diameter ratio. For that reason, a broader frequency content is expected to be found in the loading harmonics at this strip [see Figs. 27 and 28 in Rendon *et al.* (2024)], leading to a larger acoustic signature at the BPF and its harmonics. Finally, a good agreement is found between the simulation and the model for the tangential component at $r/r_{tip} = 0.9$. However, the axial component, obtained from the LBM simulation, presents an opposite behavior when compared with the rest of the results and the model. Note that the blade potential-interaction model is unable to predict the unsteady nature of the blade tip region, as it is a two-dimensional model that does not account for three-dimensional flow features present at this particular location. Moreover, the model cannot take into account any changes in the flow regime, i.e., flow separation.

To verify such a behavior suspected at the tip, Fig. 4 shows on the left two instantaneous iso-surfaces of the Λ_2 criterion (second invariant of the velocity gradient tensor) colored by the normal velocity ranging from -10 to $10\,\text{m/s}$ [Fig. 4(a)], and the mean wall-pressure coefficient $C_p \equiv (p - p_{in})/(0.5\,\rho_{in}\,r_{in}\Omega)$ at two different radii r_{in} near the tip [Fig. 4(b)]. p_{in} and ρ_{in} are the pressure and density upstream of the blade at a given radius, respectively. The bottom iso-surface of Λ_2 is related to a snapshot when the blade is not interacting with the beam [center of nonshaded zone in the bottom right corner of Fig. 4(b)], while the top one is associated with the moment when the blade is just above it [center of shaded zone in the bottom right corner of Fig. 4(b)]. Figure 4(b) shows C_p calculated at $r/r_{tip} = 0.8$ (black) and $r/r_{tip} = 0.9$ (gray). The solid lines correspond to the mean value of the white zone shown in the bottom right corner, and also in Fig. 3(c), which is linked to the locations
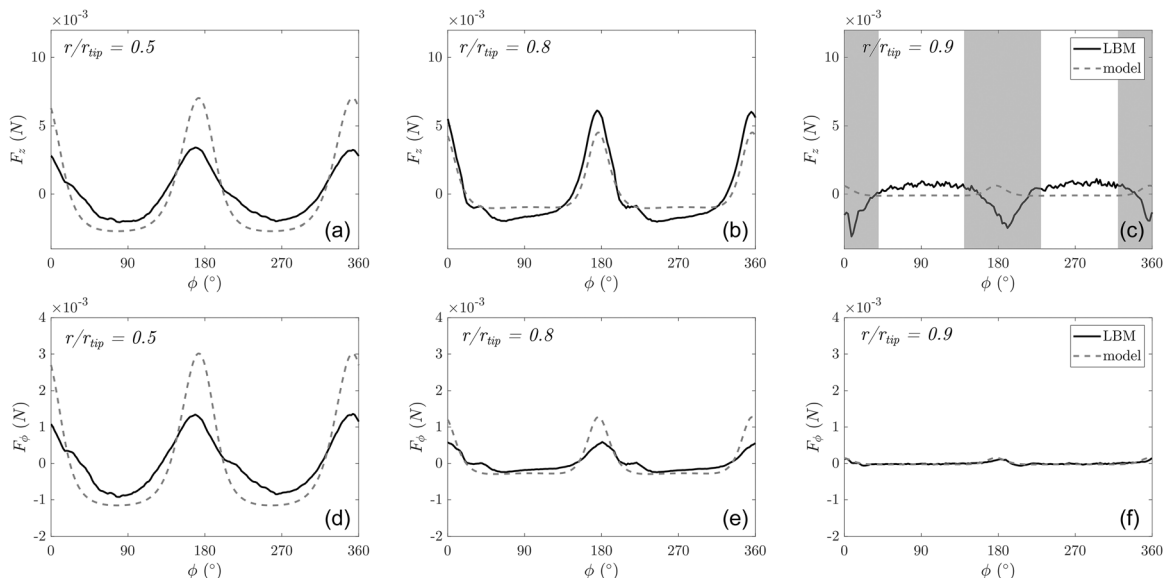

FIG. 3. Axial (a)–(c) and tangential (d)–(f) unsteady blade force signals acting on one blade, obtained from the LBM simulation and from the model, at various radial locations $r/r_{tip} = 0.5$, 0.8, and 0.9.
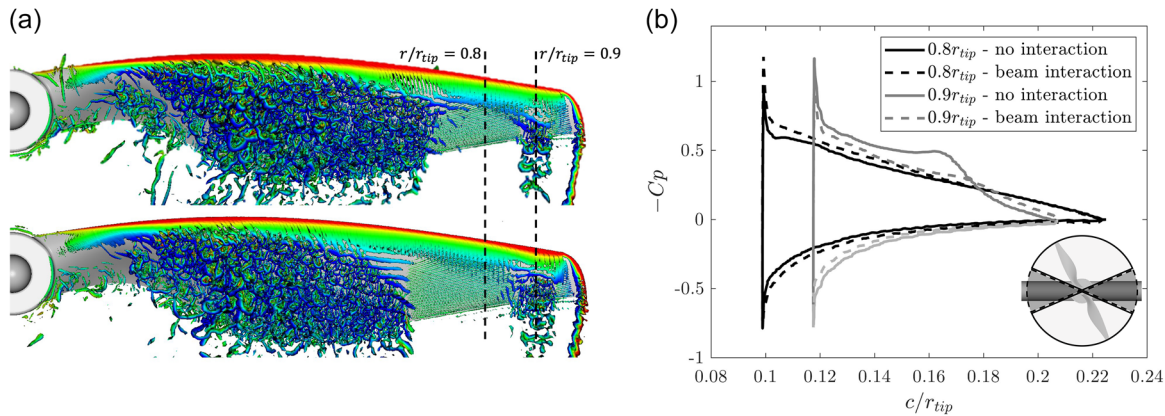
1096   J. Acoust. Soc. Am. **158** (2), August 2025

Rendón-Arredondo *et al.*

(a)

(b)

FIG. 4. (a) Top view of instantaneous Iso-surface of the Λ_2 criteria ($\Lambda_2 = 1 \times 10^8$) colored by the normal velocity for the beam-interaction (top) and no-interaction (bottom) zones. (b) Pressure coefficient (C_p) in the beam-interaction and no-interaction zones.

where the blade is not influenced by the presence of the beam (no-interaction zone). The dashed lines refer to the mean value of the gray zone shown again in the bottom right corner, and in Fig. 3(c), where the blade is influenced by the presence of the beam (beam-interaction zone). Note that the difference in chord position is due to the chord distribution of the APC $7 \times C5$-E rotor. For $r/r_{tip} = 0.8$, no major differences are seen between the beam-interaction and the no-interaction zones, neither on the C_p nor on the Λ_2 iso-surfaces. However, at $r/r_{tip} = 0.9$, the size of the leading-edge vortex (LEV) has increased and the reattachment point has moved further downstream. This is confirmed by the C_p distribution, where a plateau is seen for the no-interaction zone. The latter is caused by a flow separation that occurs around $c/r_{tip} = 0.13$, followed by a transition to turbulence at about $c/r_{tip} = 0.16$ and a reattachment point around $c/r_{tip} = 0.18$. Such a flow pattern with a reattachment point close to the trailing edge of the blade is typical of laminar separation bubbles on airfoils at similar low Reynolds numbers (Winslow et al., 2018). For the beam-interaction zone, the axial velocity decreases as a result of the presence of the beam. This induces a sudden increase in the angle of attack, taking that rotor section into the dynamic stall regime. As a consequence, the LEV size reduces, generating the decrease in thrust seen in the loading fluctuation of Fig. 3(c) and explained by the reduction in the area contained in Fig. 4(b). As expected from the near-stall condition, a decrease in thrust also leads to an increase in drag, which reduces the efficiency of the rotor in that particular time lapse. The analytical model is not able to capture these coupled interactions as it does not account for instantaneous changes, e.g., the reduction in the induced velocity due to the presence of the beam.

B. Unsteady beam forces

Figure 5 presents the signals for the unsteady forces acting on one beam, in the axial [Figs. 5(a)–5(c)] and tangential directions [Figs. 5(d)–5(f)], at various radial locations ($r/r_{tip} = 0.5$, 0.8, and 0.9). In a similar way to Sec. V A, the

radial component is not presented here. It is found to be two orders of magnitude lower when compared to the other two components in the LBM simulation, showing the validity of the 2D beam potential-interaction model. The black line reports the results obtained by the LBM simulation, while the gray dashed line shows the results obtained with the beam potential-interaction model. At all radial locations and for both axial and tangential components, the model gives very similar results to the LBM simulation. Each beam undergoes two fluctuations per rotation, induced by the passage of the two blades. At $r/r_{tip} = 0.5$, loading fluctuations are wider and lower than at $r/r_{tip} = 0.8$, where they are sharper, causing a broader frequency content in the force harmonics as already stated before. At $r/r_{tip} = 0.9$, levels are lower but the width of the fluctuations is comparable. In a recent similar study (Vella et al., 2024), the rotor (NACA 0012 profile, constant chord $c = 25$ mm, constant pitch of $10°$) and the beam diameter ($D_b = 20$ mm) are significantly different. In turn, the fluctuations of the unsteady forces acting on the beam in Vella et al. (2024) obtained with an implicit large eddy simulation (iLES), show a specific pattern: two sharp peaks for each rotor-beam interaction. The present LBM results only exhibit one single peak at each fluctuation. The two peaks obtained in Vella et al. (2024) can be traced to the pressure distribution around the blade section (NACA 0012 profile), which is likely different for the present APC blade (NACA 4412 profile) as the pressure distribution depends on the camber and thickness of the corresponding blade section, as well as the angle of attack. The latter is directly related to the flow features, i.e., the rotational speed and the axial induced velocity at the corresponding radial location. Moreover, even if the pressure distribution is important to obtain the right fluctuation pattern, the chord-to-beam diameter ratio c/D_b also seems crucial. The case studied in Vella et al. (2024) has a larger chord-to-beam diameter ratio compared to the present case (1.25 versus 0.4). This in turn changes the fluctuation patterns, and therefore the distribution of loading harmonics. The present APC blade tip can be considered as aerodynamically compact compared to the beam.

J. Acoust. Soc. Am. **158** (2), August 2025
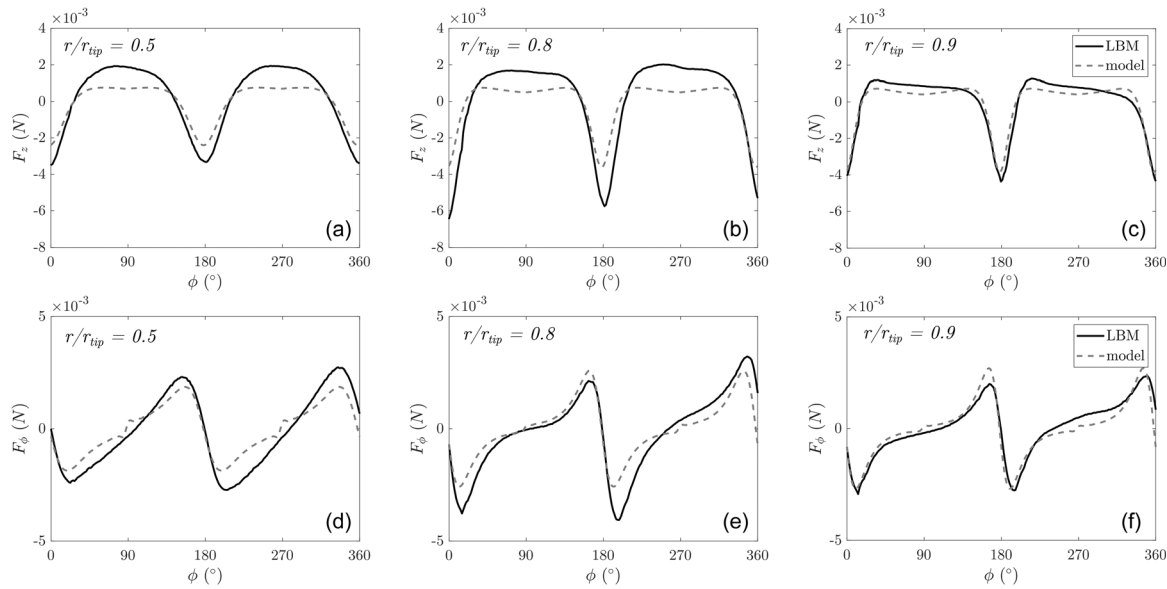
Rendón-Arredondo et al.   1097

FIG. 5. Axial (a)–(c) and tangential (d)–(f) unsteady force signals acting on one beam, obtained from the LBM simulation and from the model, at various radial locations $r/r_{tip} = 0.5$, 0.8, and 0.9.

VI. ACOUSTIC RESULTS

The far-field acoustic spectra at some specific locations are first reported, followed by the corresponding 3D directivities. As aforementioned, the presented experimental spectrum is obtained by averaging spectra on 1 s time-window, with a resolution of 1 Hz. Regarding the results of the LBM simulation, after performing the FW-H analogy, the acoustic pressure is obtained at all the microphone locations. The acoustic spectra are computed using the fast Fourier transform (FFT) with a Hanning window applied on 2 time-windows using 60% overlap and an amplitude correction factor of 2. The frequency resolution is then 7.56 Hz.

Figure 6 presents the sound pressure level (SPL) spectra, at $\phi_{exp} = 90°$, $\theta_{exp} = 45°$ for a source-observer distance of $R = 1.2$ m. The microphone position is depicted using the black dot in the inset of each figure. Figure 6(a) first compares the experiment (black line) with both the simulation and the model. The numerical results are plotted as the continuous gray line and circle markers at the BPF (214 Hz) and harmonics, while the model predictions are shown by gray square markers at the same location. The former are obtained from the application of the FW-H acoustic analogy and the latter is obtained by applying the models described in Secs. IV A and IV B. The rotor noise prediction is the sum of thickness, steady-loading, and unsteady-loading noise contributions. The results obtained from all approaches show a good general agreement. For the first five harmonics of the BPF, an overprediction is seen for the analytical model while the LBM simulation matches the tone levels obtained in the experiments. At higher frequencies, the LBM under-predicts tone levels. Moreover, there is also a good match between the numerical and experimental data when comparing the broadband noise contribution. This suggests that the flow transition over the rotor blades is properly captured. The roll-off present around 6 kHz is

related to the cut-off frequency, associated with the aforementioned sampling frequency of the surface pressure in the LBM. Figure 6(b) then presents the separate noise contributions of the rotor (red) and of the diametrical beam (blue), together with the noise measured in the experiments (black). In general, there is good agreement between the results obtained from the simulation and those calculated by means of analytical models. The spectrum presents a strong tonal component that dominates up to $10 \times$ BPF. A systematic overprediction of the tone levels is seen across all the frequency range for the rotor. The latter can be first traced to the overprediction of the blade loading harmonics in Sears's model (Rendon et al., 2024). Moreover, other phenomena are not explicitly accounted for in the present analytical models. Typically, the diffraction of rotor noise by the beam and vice versa, as suggested by the significant correlation between wall-pressure fluctuations on the beam and the far-field sound shown in Fig. 24 of Rendon et al. (2024), is ignored. It also influences the surface pressure on the rotor that is propagated to the far field. The importance of diffraction in compact rotor-beam configuration still needs to be investigated, as discussed in Roger et al. (2023). An additional hump similar to what Gojon et al. (2023) already observed is also visible in the experimental mid-frequency range. However, its peak frequency is different between the experimental and numerical results, as for the former it is centered at $10 \times$ BPF while for the latter it is at $13 \times$ BPF. In the present case, the hump is clearly related to the unsteady-loading noise of the rotor. Using filtered wall-pressure fluctuations in the frequency range of interest, Rendon et al. (2024) also relate this hump in the far-field noise to the breakdown of the LEV and to trailing-edge noise. Furthermore, the model tends to underpredict the tone levels related to the beam noise up to $3 \times$ BPF where the agreement of the results improves significantly. Contrary to
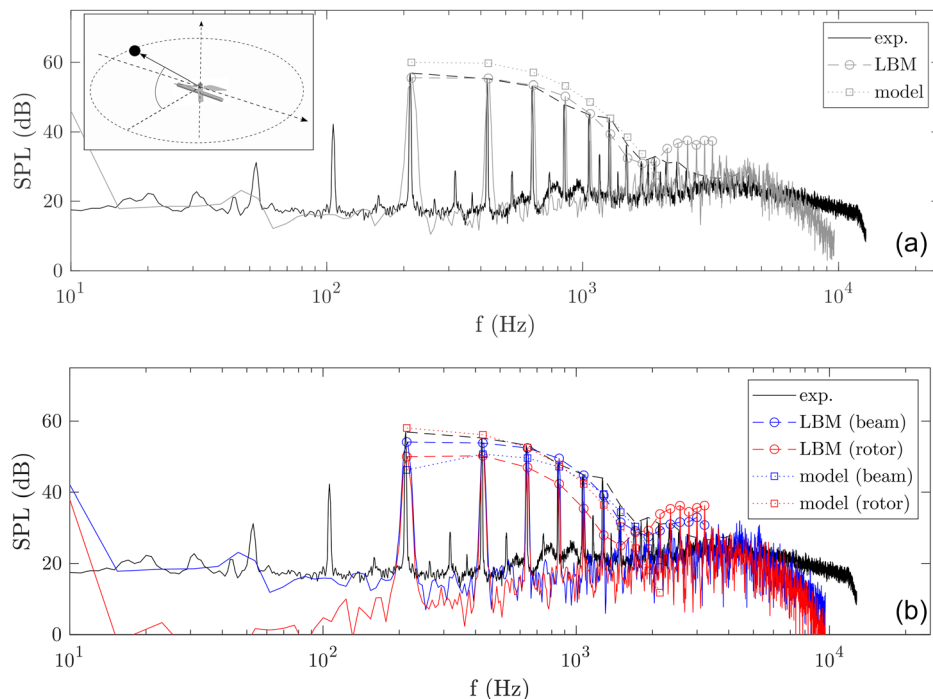
1098   J. Acoust. Soc. Am. **158** (2), August 2025

Rendón-Arredondo *et al.*

FIG. 6. Sound pressure level (SPL) spectra and tone levels at $\phi_{exp} = 90°$, $\theta_{exp} = 45°$. Results from the models and numerical simulations are compared to that of experiments: (a) overall noise, (b) split noise contributions.

the experiment in Vella *et al*. (2024), beam noise in the LBM simulation and unsteady loading noise in the analytical model are found to be the main contributors to the far-field noise spectra at the BPF, stressing that steady-loading noise and thickness noise radiated by the rotor are not dominant for this particular configuration. The blade design parameters appear as crucial. Additionally, there is no such visible hump of the tone envelope centered at $5 \times$ BPF as in the reference. This is most likely caused by the different pressure distributions around the blade profiles and the different chord-to-beam diameter ratios. Similar results are found in other directions.

Figure 7 reports the 3D directivities of the total far-field noise radiated by the rotor-diametrical beam configuration at $3 \times$ BPF, as well as the separate contributions of the rotor and of the beam. Figures 7(a)–7(c) are obtained from the LBM simulations, while Figs. 7(d)–7(f) are computed with the model. The rotor disk plane is represented by the dashed black circle, and the diametrical beam by the thick black line. The total noise directivities, presented in Figs. 7(a) and 7(d), are in good agreement. Minimum levels are obtained mainly near the rotor disk plane, and maximum levels are aligned with the rotor axis. The 3D rotor noise directivities, obtained from the LBM simulation and with the rotor noise model, are presented in Figs. 7(b) and 7(e), respectively. Both have the same 3D shape, i.e., a dipole-like pattern with a minimum level near the rotor disk plane, stressing that the unsteady loading noise is the main contributor to the rotor noise at $3 \times$ BPF. However, the noise level calculated with the model is a few dB higher compared to the LBM simulation with an average difference of 14%. This behavior is in agreement with the SPL spectra in Fig. 6(b). The corresponding 3D beam noise directivities are reported in Figs. 7(c) and 7(f). Similar 3D shapes are observed between

the LBM simulation and the beam noise model: a dipole-like pattern with minimum levels describing a wavy line around the rotor disk plane. Yet, the noise level obtained with the model is slightly lower compared to the level of the LBM simulation with an average difference of 5%, which is smaller than the one obtained for the rotor noise and is consistent with the results in Fig. 6(b).

To explain this low-noise level wavy line obtained in Figs. 7(c) and 7(f), Fig. 8 presents the 3D phase directivities, obtained with the beam noise model, at $3 \times$ BPF. On the one hand, Fig. 8(a) stands for a radial beam configuration, i.e., a single interaction with the beam for a blade revolution. The bottom inset shows the phase directivity from a back view angle, and the top inset shows the 3D noise directivity obtained for a radial beam configuration. On the other hand, Fig. 8(b) corresponds to a diametrical beam configuration, i.e., two interactions per revolution, and as for Fig. 8(a), the bottom inset shows the phase directivity from a back view angle, and the top inset shows the present 3D noise directivity. The color scale, going from 0 to π rad, represents the absolute phase value of the complex acoustic pressure obtained with the beam potential-interaction noise model. For the radial beam configuration, the phase of the upper part of the 3D directivity is smaller than $\pi/2$, while for the lower part it is larger. Near the rotor disk plane highlighted by a black dashed line, the absolute value of the phase is around $\pi/2$. Looking at the front and back views presented in Fig. 8(a), this iso-phase value draws a wavy line around the rotor disk plane, with a clear boundary between the 0-phase (dark blue) and the π-phase (dark red) areas. This mathematically induces a similar wavy pattern for the diametrical beam case in Fig. 8(b). Yet, as shown in Fig. 9 presenting a cut of the phase spheres in the rotor disk plane, the transitions in phase are much sharper for the diametrical
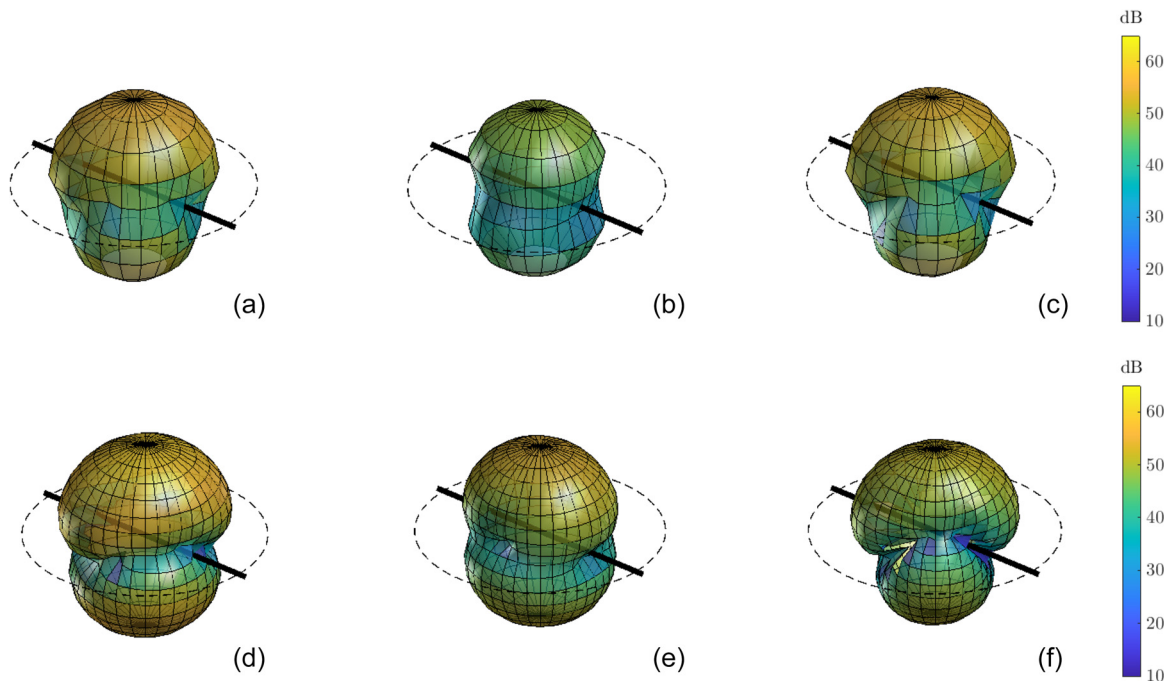
J. Acoust. Soc. Am. **158** (2), August 2025

Rendón-Arredondo *et al.* 1099

FIG. 7. 3D noise directivities of the two-bladed rotor with the diametrical beam downstream, at $3 \times$ BPF. Results from LBM simulations (a)–(c) are compared to the model (d)–(f): full noise (a) and (d); rotor contribution (b) and (e); beam contribution (c) and (f).

beam than for the radial one. Consequently, the 3D noise directivity in Figs. 7(c) and 7(f) exhibits a wavy pattern for the diametrical beam, whereas it is hardly seen for the radial beam configuration in Fig. 8(a). The latter mostly exhibits a minimum aligned with the beam axis. Moreover, following the sharp wavy line around the sphere in Fig. 8(b), four spots corresponding to an absolute phase value of $\pi/2$ are visible. Knowing that interaction of the two-bladed rotor with the diametrical beam generates source-modes of even orders (Roger *et al.*, 2023) [i.e., $n = mB - kn_b = 2(m - k)$ as $B = 2$ and $n_b = 2$], the radiation of the mode $n = 4$ is therefore expected. The excitation of mode $n = 4$ leads to four minimum noise level locations [see Figs. 7(c) and 7(f)].

This comes from the dipole-like emission of each beam, which cancels out as they are equivalent in amplitude but opposite in phase.

VII. CONCLUSIONS

Experiments, high-fidelity LBM simulations, and analytical models have been described in the present study, with the aim of clarifying various intricate aeroacoustic mechanisms involved in a rotor-beam configuration, which is a typical subsystem encountered in multicopter architectures.

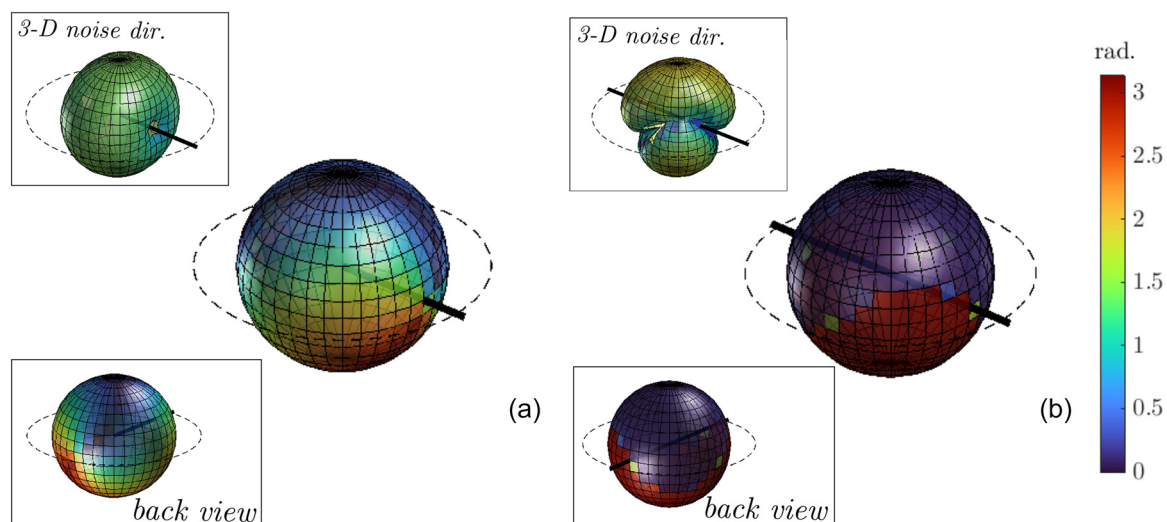Aerodynamic results obtained from the LBM simulation and the models have been first compared. The unsteady

FIG. 8. 3D phase directivities, at $3 \times$ BPF, for a radial beam configuration (a), versus a diametrical beam configuration (b).
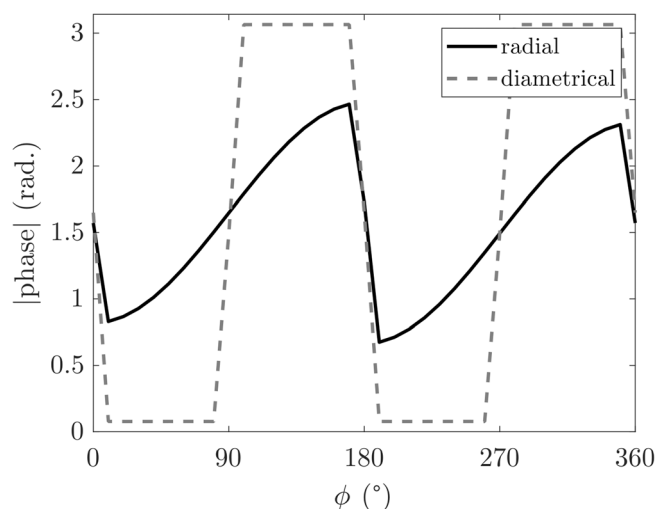
Rendón-Arredondo *et al.*

FIG. 9. Evolution of the absolute phase value along the azimuth, for a radial beam configuration (black line) versus a diametrical beam configuration (gray dashed line), in the rotor disk plane.

loading on the blades and the beam shows an overall good agreement. For the beam loading, the LBM and the 2D beam potential-interaction model give very similar results. While the pressure distribution is critical for predicting these loading fluctuations, the chord-to-beam diameter ratio (c/D_b) also plays a significant role in this prediction. However, for the blade loading, some 3D flow features and changes in the flow regime (LSB) typical of low-Reynolds number airfoils and near-stall conditions lead to some differences between the LBM and the 2D blade potential-interaction model, specifically near the tip radius.

Acoustic results have then been assessed. For the SPL spectra, the LBM simulation and the total analytical noise prediction by the model are in good agreement with the measurements both in terms of levels and spectral shape. Indeed, the LBM manages to capture not only the tonal noise but also the broadband noise quite well. When the rotor and beam contributions are split, the LBM and the models do not always behave similarly, specifically at the BPF. For the LBM, the beam contribution is prominent at this frequency, while the rotor contribution dominates according to the models. Note, however, that for both LBM simulation and analytical model, the unsteady loading noise radiated by the rotor is prominent at the BPF, compared to the steady loading noise and the thickness noise. This is different from the NACA-0012 blade case considered in Vella et al. (2024). The observed overprediction of the rotor noise by the analytical model is mostly explained by a higher amplitude found in the loading fluctuations obtained with the blade potential-interaction model based on Sears's response function. Acoustic diffraction from both system components seen in the LBM results but presently not modeled can also contribute to this discrepancy. Looking at the 3D noise directivities, at $3 \times$ BPF, similar conclusions can be drawn. Good overall agreement of the beam and total noise is found between the LBM, the analytical models, and the experiments, noticeably in terms of shape. A dipole-like

pattern with minimum levels featuring a wavy line around the rotor disk plane is also found, for both the LBM and the analytical model. Such a wavy line of minimum noise levels is expected when looking at the 3D phase directivity obtained from the complex acoustic pressure radiated by one beam.

In summary, the analytical models, the high-fidelity LBM simulation and the experiments yield a good comparison of both aerodynamic and acoustic results, despite some limitations in the models and a missing contribution related to the sound-scattering effects from the diametrical beam and the blades. In the present limit of small chord-to-beam diameter ratios, the rotor blade can be seen as a point source interacting with the beam at every radius because its cross section profile is aerodynamically compact. Unsteady loading is the dominant noise source of tonal noise at all BPF harmonics.

AUTHOR DECLARATIONS
Conflict of Interest

The authors have no conflicts to disclose.

DATA AVAILABILITY

The data that support the findings of this study are available from the corresponding author upon reasonable request.

Amiet, R. K. (**1975**). "Acoustic radiation from an airfoil in a turbulent stream," J. Sound Vib. **41**(4), 407–420.

Bhatnagar, P. L., Gross, E. P., and Krook, M. (**1954**). "A model for collision processes in gases. I. Small amplitude processes in charged and neutral one-component systems," Phys. Rev. **94**(3), 511–525.

Casalino, D. (**2003**). "An advanced time approach for acoustic analogy predictions," J. Sound Vib. **261**(4), 583–612.

Casalino, D., Romani, G., Zhang, R., and Chen, H. (**2022**). "Lattice-Boltzmann calculations of rotor aeroacoustics in transitional boundary layer regime," Aerosp. Sci. Technol. **130**, 107953.

Chen, H., Chen, S., and Matthaeus, W. H. (**1992**). "Recovery of the Navier-Stokes equations using a lattice-gas Boltzmann method," Phys. Rev. A **45**(8), R5339.

Chen, H., Orszag, S. A., Staroselsky, I., and Succi, S. (**2004**). "Expanded analogy between Boltzmann kinetic theory of fluids and turbulence," J. Fluid Mech. **519**, 301–314.

Doué, N., Gojon, R., and Jardin, T. (**2023**). "Numerical investigation of the acoustics radiation of a two-bladed rotor in interaction with a beam," in *Proceedings of the 6th Symposium on Fluid-Structure-Sound Interactions and Control*, Busan, South Korea, pp. 169–176.

Farassat, F., and Succi, G. P. (**1980**). "A review of propeller discrete frequency noise prediction technology with emphasis on two current methods for time domain calculations," J. Sound Vib. **71**(3), 399–419.

J. Acoust. Soc. Am. **158** (2), August 2025

Rendón-Arredondo *et al.*   1101

Ffowcs Williams, J. E., and Hawkings, D. L. (**1969**). "Theory relating to the noise of rotating machinery," J. Sound Vib. **10**(1), 10–21.

Gojon, R., Jardin, T., and Parisot-Dupuis, H. (**2021**). "Experimental investigation of low Reynolds number rotor noise," J. Acoust. Soc. Am. **149**(6), 3813–3829.

Gojon, R., Parisot-Dupuis, H., Mellot, B., and Jardin, T. (**2023**). "Aeroacoustic radiation of low Reynolds number rotors in interaction with beams," J. Acoust. Soc. Am. **154**, 1248–1260.

Gutin, L. (**1948**). "On the sound field of a rotating propeller," Phys. Z. Sowjetunion **9**(1), 20030068996.

Hanson, D. B., and Parzych, D. J. (**1993**). "Theory for noise of propellers in angular inflow with parametric studies and experimental verification," Contractor Report No. NAS 1 26, 4499, NASA, Lewis Research Center.

Jo, Y., Jardin, T., Gojon, R., Jacob, M. C., and Moschetta, J.-M. (**2019**). "Prediction of noise from low Reynolds number rotors with different number of blades using a non-linear vortex lattice method," in *Proceedings of the 25th AIAA/CEAS Aeroacoustics Conference*, Delft, The Netherlands, Paper AIAA 2019-2615.

Kim, S. J., Hwang, Y.-H., Myong, R. S., and Lee, H. (**2024**). "Interactional aerodynamics and acoustics of a rotor with an airframe in hover," Phys. Fluids **36**(1), 017121.

Lauzon, J. S., Vincent, J., Pasco, Y., Grondin, F., and Moreau, S. (**2023**). "Aeroacoustics of drones," in *Proceedings of the 29th AIAA/CEAS Aeroacoustics Conference*, San Diego, CA, Paper AIAA 2023-4524.

Leishman, J. G. (**2006**). *Principles of Helicopter Aerodynamics*, 2nd ed. (Cambridge University Press, Cambridge, UK).

Li, Y., Shock, R., Zhang, R., and Chen, H. (**2004**). "Numerical study of flow past an impulsively started cylinder by the lattice-Boltzmann method," J. Fluid Mech. **519**, 273–300.

Lowson, M. V. (**1969**). "Theoretical studies of compressor noise," Contractor Report No. WR-68-15, NASA Langley Research Center.

Moreau, S., and Sanjose, M. (**2016**). "Sub-harmonic broadband humps and tip noise in low-speed ring fans," J. Acoust. Soc. Am. **139**(1), 118–127.

Parry, A. B. (**1988**). "Theoretical prediction of counter-rotating propeller noise," Ph.D. thesis, University of Leeds, Leeds, UK.

Rendon, J., Arroyo Ramo, A., Moreau, S., and Roger, M. (**2024**). "A numerical and analytical approach of the sound-scattering effects in rotor-strut interaction noise of small-size drones," in *Proceedings of the 30th AIAA/CEAS Aeroacoustics Conference*, Rome, Italy, Paper AIAA 2024-3047.

Rendon-Arredondo, J., Moreau, S., Gojon, R., and Bauerheim, M. (**2024**). "LBM and iLES comparison for the aerodynamic and acoustic characteristics of a low-speed rotor," in *Proceedings of the 30th AIAA/CEAS Aeroacoustics Conference*, Rome, Italy, Paper AIAA 2024-3048.

Roger, M., Vella, E., Rendon-Arredondo, J., Moreau, S., and Pereira, A. (**2023**). "Aerodynamic and sound-scattering effects in rotor-strut interaction noise of small-size drones," in *Proceedings of the 29th AIAA/CEAS Aeroacoustics Conference*, San Diego, CA, Paper AIAA 2023-4523.

Romani, G., Grande, E., Avallone, F., Ragni, D., and Casalino, D. (**2022**). "Performance and noise prediction of low-Reynolds number propellers using the lattice-Boltzmann method," Aerosp. Sci. Technol. **125**, 107086.

Sanjose, M., Moreau, S., Pestana, M., and Roger, M. (**2017**). "Effect of weak outlet-guide-vane heterogeneity on rotor–stator tonal noise," AIAA J. **55**(10), 3440–3457.

Sears, W. R. (**1941**). "Some aspects of non-stationary airfoil theory and its practical application," J. Aeronaut. Sci. **8**(3), 104–108.

Shenoy, D., Gojon, R., Jardin, T., and Jacob, M. (**2024**). "Aerodynamic and acoustic study of a small scale lightly loaded hovering rotor using large eddy simulation," Aerosp. Sci. Technol. **150**, 109219.

Teixeira, C. M. (**1998**). "Incorporating turbulence models into the lattice-Boltzmann method," Int. J. Mod. Phys. C **09**(08), 1159–1175.

Vella, E., Gojon, R., Parisot-Dupuis, H., Doué, N., Jardin, T., and Roger, M. (**2024**). "Mutual interaction noise in rotor-beam configuration," in *Proceedings of the 30th AIAA/CEAS Aeroacoustics Conference*, Rome, Italy, Paper 2024-3318.

Winslow, J., Otsuka, H., Govindarajan, B., and Chopra, I. (**2018**). "Basic understanding of airfoil characteristics at low Reynolds numbers (104–105)," J. Aircraft **55**(3), 1050–1061.

Wu, Y., Kingan, M., and Go, S. (**2022**). "Propeller-strut interaction tone noise," Phys. Fluids **34**, 055116.

Yakhot, V., and Orszag, S. A. (**1986**). "Renormalization group analysis of turbulence. I. Basic theory," J. Sci. Comput. **1**(1), 3–51.

Zawodny, N. S., and Boyd, D. D. (**2017**). "Investigation of rotor–airframe interaction noise associated with small-scale rotary-wing unmanned aircraft systems," J. Am. Helicopter Soc. **65**(1), 012007.

Zawodny, N. S., Boyd, D. D., Jr., and Burley, C. L. (**2016**). "Acoustic characterization and prediction of representative, small-scale rotary-wing unmanned aircraft system components," in *American Helicopter Society (AHS) Annual Forum*, West Palm Beach, FL.

14 August 2025 15:38:11